Exploring hydrophobic surface modifications in silica and alumina nanomaterials☆☆

Erica Rebba, Pavlo Ivanchenko [1], Simone Bordignon, Ola El Samrout, Michele R. Chierotti, Federico Cesano, Gloria Berlier [*]

Department of Chemistry, NIS Centre of Excellence and INSTM Reference Center, University of Torino, via P. Giuria 7, 10125 Torino, Italy

A B S T R A C T

Superhydrophobic materials have attracted significant attention in various applications including leather manufacturing, water-resistant textiles, self-cleaning surfaces, anti-icing coatings, etc... In the present work, we elucidated the functionalization of silica nanoparticles using isostearic acid, a cheap, non-toxic and highly branched molecule, substituting the conventional toxic fluorinated molecules, in comparison with the alumina counterpart and commercial hydrophobic materials. In this respect, the performance of isostearic acid is compared to the commercially used hexamethyldisilazane, a rigid and bulky moiety of high toxicity and environmental persistence. The functionalized surfaces were characterized by infrared spectroscopy, nuclear magnetic resonance spectroscopy, N_2 physisorption, field emission scanning electron microscopy, and thermogravimetric analysis. Microgravimetric and microcalorimetric measurements were also used to describe the surface interaction with water, while the water-repellency at the macroscopic level was monitored through contact angle measurements. Both silica surfaces functionalized with isostearic acid and hexamethyldisilazane show a collective superhydrophobic behavior, but the flexibility of the isostearic acid chains, bonded in low surface density (0.7 units per nm^2) through alkyl chains, allow for diffusion of water vapor at the molecular level, while this is not observed in the hexamethyldisilazane case due to the smaller molecular size of the rigid moiety, coupled to a higher surface density (3.5 units per nm^2). The results revealed that a material does not necessarily expose micro-nano hierarchical structures to reach an ultimate waterproof capability with a contact angle higher than 150°.

1. Introduction

Superhydrophobicity, a commonly observed phenomenon that consists in reaching an ultimate waterproof capability, has attracted a significant deal of importance in a wide range of industrial and commercial applications [1], such as self-healing coatings [2], food-packaging [3], photographic field, pesticides production [4], painting [5], anti-corrosion coatings [6], anti-icing [7], and leather manufacturing [8]. Superhydrophobicity is also a required characteristic for materials used in solar energy panels, exterior glass and heat transfer surfaces in air conditioning equipment [9]. While the deposition of a droplet of water on a hydrophobic surface generates an angle between the liquid-solid and liquid-vapor interfaces, called contact angle, between 90 and 150°, a superhydrophobic surface shows a contact angle greater

than 150° [5]. The basic principles of the high water contact angle and the self-cleaning properties of superhydrophobic materials are well-known in nature, with the so-called "Lotus effect" [10,11]. Most of the research works based on the production of superhydrophobic coatings are inspired by the characteristics of Lotus leaves; in fact, they naturally combine a low-surface energy with the exhibition of micro-nano hierarchical structures on the surface, forming roughness grooves, that can trap air and thus protect the surface from water [10, 12].

To mimic this effect, a variety of surface modification strategies and several molecules exposing hydrophobic moieties are employed in the preparation of water-repellent coatings with low-surface energy and high roughness [13–15]. Nowadays, perfluoroalkyls (PFAs) and their derivatives have been used in various manufacturing fields to satisfy the

hydrophobic requirements of a large number of consumer products [16–18]. The PFAs term refers to more than 4000 substances, consisting of a carbon backbone with fluorine atoms attached to alkyl chains of different lengths. According to literature, a wide employment of fluoroalkylsilane moieties has been reported for the functionalization of silica nanoparticles to reach hydrophobic behaviors [19–22]. However, many research studies have reported evidences on the detection of PFAs in air, water, and soil, representing a major contributor in the environment pollution [17,23,24]. In addition, studies have shed light on the potential risk of PFAs on human health, being a persistent organic substance that accumulates in human body through inhalation, water, and food ingestion, resulting in severe diseases [25,26].

The growing awareness of environmental issues and social challenges have been strongly pushing recent research works to study the use of new sustainable, fluorine-free materials for the production of waterproof coatings. One promising route, as an eco-friendly alternative, has been reported through the use of oxide nanoparticles (e.g. alumina, silica, etc...) with various surface modifiers of different alkyl chains length and branching moieties to satisfy waterproofing qualities [1,14,27,28]. Alumina is a crystalline oxide, with high thermal and chemical stability, widely used in catalysis as support. The thermodynamically stable phase is α-Al_2O_3 (corundum). However, in the practical language of catalysis and surface chemistry the term alumina normally refers to the so-called transition alumina (γ, δ, θ, η), which are metastable phases of low crystallinity (small particle size) characterized by high surface area and open porosity. The surface of alumina is characterized by a distinct Lewis acid nature related to undercoordinated surface Al^{3+} sites, which confer to the material a positive surface charge [29]. Alumina displays a high resistance and durability compared to other materials including high temperature and corrosive environments which makes it a good candidate for various industrial applications including waterproofing ones [30,31]. Silica, on the other hand, is an amorphous material, usually characterized by a high surface area related to small particle size, conferring to the material an intrinsic porosity. The main functional groups on the surface of silica are mildly acidic Si–OH groups, the concentration and distribution of which can be tuned by synthesis and thermal treatments, thus affecting its hydrophobic/hydrophilic macroscopic behavior [32–36].

In particular, modified silica nanoparticles were studied as hydrophobic materials for clothes, shoes, papers, glass, and other consumer goods of industrial interest [37]. However, potential obstacles in the supply of some commercially available materials for the functionalization of silica nanoparticles and the required precaution to avoid health and risks for the workers in the use of some kind of hazardous alkylsilanes, such as hexamethyldisilazane (HMDS) [38,39], led to the exploitation of new safer strategies for the production and application of hydrophobic nanoparticles [27,40]. The surface of silica nanoparticles consists of an interconnection of siloxane bridges Si–O–Si, broken up by sites of silanol groups Si–OH that are formed by an incomplete condensation of silicic acid monomers during nanoparticle synthesis [32]. Silanol groups are responsible for the hydrophilic/hydrophobic behavior of silica [34], since they can interact with different molecules through hydrogen bonds (H-bonds). The surface of silica is well-known for its potential conjugation with different molecules through simple synthetic procedures and commercially available reactants; therefore, it is useful, in the exploitation of new waterproofing strategies, to take advantage of its ability to form covalent bonds, avoiding the desorption of hydrophobic molecules from the surface and controlling the number and orientation of anchored moieties [41].

Isostearic acid (ISOST) is a commercially available hydrophobic molecule due its highly branched alkyl chain, which is cost-effective, safe, non-toxic, and biodegradable [42]. ISOST has been used at laboratory scale for the functionalization of alumina nanoparticles owing to their high chemical stability [30], following a well-defined protocol [40]. Starting from this know-how, we have focused our attention to silica nanoparticles for different reasons. First, silica surface can be

functionalized with amino groups to covalently bond ISOST, resulting in a more robust and stable interaction with respect to the Coulombic interaction between the carboxylate group of ISOST and surface cations exploited for the surface functionalization of alumina nanoparticles [37]. Secondly, using silica nanoparticles instead of alumina could represent a path to reach sustainability: silica has already been widely used in various industrial and commercial applications owing to its large availability and low cost; the functionalization with hydrophobic moieties on the surface of the already applied material could avoid the use of another compound in the treatment to deliver additional waterproof qualities.

In the present work, we aim to study the functionalization of commercial silica nanoparticles [43,44] using ISOST for waterproofing purposes. The obtained functionalized silica surfaces were investigated and compared to the benchmarking alumina materials through a detailed characterization of the dimensional, morphological, and surface features of the silica nanomaterials using several complementary techniques including N_2 physisorption, thermogravimetric analysis (TGA), transmission Fourier transform infrared (FTIR) spectroscopy, near IR, FESEM, and solid-state NMR (SSNMR) measurements. In addition, the capacity of the repellence toward water droplets was monitored at the macroscopic level by contact angle measurements while the adsorption capacity toward water vapor was investigated by microgravimetric and microcalorimetric measurements. The efficiency of the selective ISOST coating used was compared with benchmark HMDS, a rigid molecule that has only secondary amine and CH_3 groups in its structure, employed for the functionalization of commercial hydrophobic silica material.

2. Experimental section

2.1. Materials

Four commercial oxides with well-defined properties were purchased from Evonik. Namely, these are:

- Aeroxide AluC, hereafter referred to as AluC, a highly dispersed fumed alumina with γ-δ crystalline structure;
- Aeroxide AluC805, hereafter referred to as AluC850, a highly dispersed fumed alumina hydrophobized with an organosilane (C8 type), which was used as a reference material;
- Aerosil 300, hereafter labelled as A300, a hydrophilic fumed silica obtained by $SiCl_4$ flame pyrolysis;
- Aerosil R 812 (hereafter AR812), a fumed silica treated with hexamethyldisilazane (HMDS), which was used as a reference material.

(3-Aminopropyl)triethoxysilane (APTS, purity: 99 %), hydrochloric acid (37 %); thionyl chloride, 2-propanol, ethanol, toluene, dichloromethane, methanol, and deuterated water (99.9 atom%D) were purchased from Merck. Isostearic acid (isoC$_{17}$H$_{35}$)COOH (ISOST, a highly branched carboxylic acid) was purchased from Nissan Chemical Corporation. Thionyl chloride was subjected to distillation before use to avoid the presence of water during the reaction. Milli-Q and distilled water were used for the functionalization and washing, respectively.

2.2. Functionalization of AluC with ISOST

AluC was functionalized with ISOST following a literature procedure [40]. Namely, 1 g of AluC nanoparticles was refluxed overnight with 470 mg of ISOST in 100 mL of toluene at 398 K. The amount of ISOST was calculated on an excess by weight of 10 times, starting from the amount required to cover the surface with 1 ISOST per nm^2 (47 mg). The functionalized nanoparticles (Aluc-ISOST) were then centrifuged and washed with 2-propanol (2 × 50 mL, 10,000 rpm, 10 min) and ethanol (1 × 50 mL, 10,000 rpm, 10 min); the washed nanoparticles were dried overnight in oven at 323 K.

2.3. Functionalization of A300 with APTS

A300 was functionalized with APTS, as an intermediate agent necessary to bond covalently ISOST. The reaction proceeds by partial or total hydrolysis of the triethoxy groups of the aminating agent, with a consequential reaction with surface silanol groups.

Silica nanoparticles were magnetically stirred for 4 h at room temperature (r.t.) in an acidic aqueous solution (HCl 0.01 M), before adding APTS following different molar APTS:SiOH ratios (5:1, 10:1, 15:1), following literature procedures [45,46]. The molar ratio was calculated on the basis of the silanol surface density and specific surface area of A300 (5.6 SiOH nm^{-2} and 300 m^2 g^{-1}, see below) resulting in 2.79 $\times$ 10^{-3} SiOH moles per gram of silica.

The functionalized nanoparticles, hereafter referred to as A300-APTS, were then centrifuged and washed with distilled water (3 $\times$ 10,000 rpm). The washed material was dried overnight in oven at 323 K.

2.4. Functionalization of A300-APTS with ISOST

In order to increase the reactivity towards amino groups on the surface of silica, ISOST was previously modified into isostearyl chloride. 2.6 mmol of ISOST was solubilized in 4 mL of thionyl chloride, under stirring for 3 h at r.t. Thionyl chloride was then removed through vacuum distillation; further distillations (3–4 times) were carried out adding each time 5 mL of dichloromethane, in order to completely remove the reactant. After the distillations, isostearyl chloride was obtained as a light-yellow oil, with a yield of 99.6 %. Subsequently, A300-APTS nanoparticles (1 equivalent), isostearyl chloride (3 equivalents) and sodium bicarbonate (6 equivalents) were added together in 10 mL of dichloromethane. The reagents were magnetically stirred at r.t. for 4 h.

The functionalized nanoparticles, referred to as A300-APTS-ISOST, were then centrifuged and washed with dichloromethane (3 $\times$ 10 mL, 5000 rpm, 5 min), methanol (2 $\times$ 10 mL, 5000 rpm, 5 min) and water (2 $\times$ 10 mL, 5000 rpm, 5 min). The washed material was dried overnight in oven at 323 K.

2.5. Specific surface area (SSA$_{BET}$) measurements

The texture properties were determined by N$_2$ adsorption–desorption isotherms at 77 K using a Micromeritics ASAP 2020 instrument. Before measurements, the samples were outgassed at r.t. for 10 h. Surface areas were estimated using the Brunauer–Emmett–Teller (BET) method.

2.6. Thermogravimetric analysis (TGA)

TGA measurements, using TA Instruments SDT Q600, were carried to estimate the surface silanol groups density on A300, and the grafting density of the hydrophobic molecules on the commercial hydrophobic samples (AluC805 and AR812) and the functionalized samples (AluC-ISOST, A300-APTS, and A300-APTS-ISOST). The samples were analyzed in powder form placing 10 mg aliquots in the sample holder. Measurements were performed under a constant air flux (0.1 L min^{-1}) with a heating rate of 10 K min^{-1} from 298 to 1273 K.

The grafting density is estimated from:

$$\left(\frac{wt\%}{100-wt\%}\right)\left(\frac{6.022\cdot10^{23}}{Mw\cdot SSA\ \cdot10^{18}}\right)$$

where *wt%* corresponds to the weight loss of the dry material, that is considering the weight measured after desorption of water around 373 K; *Mw* is the mass weight of the functionalized agents; *SSA* is the specific surface area. The surface silanol density on A300 was calculated with a similar equation multiplied by 2, where *Mw* is the mass weight of water, assuming that one water molecule is released by the condensation of two SiOH groups.

2.7. Infrared (IR) spectroscopy

IR spectra were recorded using a Bruker IFS28 spectrometer with a DTGS detector using a resolution of 4 cm^{-1} and accumulating 128 scans to obtain a good signal-to-noise ratio. The bare and functionalized materials were pressed into self-supporting pellets and inserted in a cell equipped with CaF$_2$ windows and connected to a conventional vacuum line (residual pressure $\leq$ 5.10^{-4} mbar).

The spectra were collected in situ at beam temperature (b.t., ca. 323 K), in air, and after outgassing to remove adsorbed water on the surface.

2.8. SSNMR measurements

Solid-state NMR spectra were acquired with a Bruker Avance II 400 Ultra Shield instrument, operating at 400.23, 100.63 and 79.51 MHz, respectively for ^{1}H, ^{13}C and ^{29}Si nuclei.

For ^{13}C and ^{29}Si spectra, the powder samples were packed into cylindrical zirconia rotors with 4 mm o.d. and a 80 µL volume. A certain amount of sample was collected from each batch and used without further preparations to fill the rotor. ^{13}C CPMAS spectra were acquired at r.t. at a spinning speed of 12 kHz, using a ramp cross-polarization pulse sequence with a 90° ^{1}H pulse of 3.6 µs, a contact time of 3 or 4 ms (A300-APTS-ISOST), an optimized recycle delay of 1.1 s, a number of scans in the range 63,000–223,000, depending on the sample. Direct-excitation ^{29}Si MAS spectra were acquired at r.t. at a spinning speed of 12 kHz, using a ^{29}Si 90° pulse of 6 µs, a recycle delay of 100 s and a number of scans in the range 600–1770, depending on the sample. The ^{13}C chemical shift scale was calibrated through the methylenic signal of external standard glycine (at 43.7 ppm). The ^{29}Si chemical shift scale was calibrated through the signal of external standard TMS (at 0 ppm).

2.9. Near-IR measurements

Near-IR measurements were performed in diffuse reflectance mode, using a Varian Cary 5000 UV–Vis-NIR spectrophotometer equipped with an integrating sphere. The samples were put as a self-supporting pellet in a quartz cell directly connected to a vacuum line (residual pressure < 5.10^{-4} mbar), in order to carry out the adsorption-desorption water sequences in situ. The spectra were recorded in the 8000–4000 cm^{-1} region.

2.10. Microgravimetric measurements

The microgravimetric measurements were carried out using an Intelligent Gravimetric Analyzer IGA002 (Hiden Analytical) instrument, based on an ultrahigh-vacuum (UHV) microbalance (weighing resolution of 0.2 µg) with integrated temperature and pressure control. The samples were loaded in broken pieces of a self-supporting pellet in a sealed stainless-steel reactor, heated at 303 K and outgassed overnight ($P \leq 10^{-4}$ mbar) in order to measure the sample dry weight. The measurements were carried out admitting water vapor up to 22 mbar, and H$_2$O desorption/adsorption cycles were recorded twice for each sample.

2.11. Adsorption microcalorimetric measurements

In order to calculate the heat of adsorption, microcalorimetric measurements were carried out using a heat-flow microcalorimeter (Calvet C80, Setaram, France) connected to a grease-free high-vacuum gas-volumetric glass apparatus (residual pressure $\leq$ 1.10^{-6} Torr). The pressure was monitored by a Ceramicell 0–100 Torr gauge and a Ceramicell 0–1000 Torr gauge (by Varian), following a well-established procedure described in literature [47] and which allowed determining, for subsequent small increments of water, both adsorbed amounts (n$_a$) and integral heats evolved (–Q$_{int}$), as a function of the increasing equilibrium pressure. The calorimetric outputs (–Q$_{int}$) were converted into the differential enthalpy (–q^{diff}); the differential-heat plots were

obtained by taking the middle point of the partial molar heats ($\Delta Q_{int}/\Delta n_a$, kJ.mol^{-1}) vs. n_a, the individual adsorptive doses, in order to evaluate the energy of interaction of water with the adsorption sites. The samples were introduced in a quartz cell as pieces of broken self-supporting pellets, connected to the vacuum line of the instrument for activation overnight under vacuum at 303 K. Then the measurements were carried out in situ, sending water vapor until 10 mbar, a conservative value for an effective use of the perfect gas law for data analysis.

2.12. Contact angle measurements

Contact angle measurements were performed to estimate the hydrophobicity after functionalization with ISOST of the already mentioned materials. The experiments were carried out using a Kruss DSA100 instrument, through the sessile drop method (static contact angle) on self-supporting pellets of materials, pressed at ca. 1 ton. The contact angle was measured using a drop shape analysis program, DSA3. This approach has been preferred to the Washburn method due to the limited amount of functionalized nanoparticles and related difficulties in packing the powders for the measurements, resulting in scarce reproducibility.

2.13. FESEM

The images of the materials were acquired using a FEG-SEM S9000 by Tescan. The measurements were performed with a Schottky emitter, using a resolution of 0.7 nm at 15 keV and 1.4 nm at 1 keV; the probe current was set at 10 pA and the electron beam energy at 5 keV. The analyses were carried out with an in-beam secondary electron detector. The samples were placed in the sample holder as self-supporting pellets as for contact angle measurements.

2.14. Atomic force microscopy (AFM)

AFM studies were performed in tapping mode at room temperature in air and with RH about 30 %. AFM cantilevers (Tap190Al-G, Budget-Sensors) with a length of 225 μm, probe height of 17 μm, and tip radius of 10 nm, with a resonance frequency of 190 kHz, were used. For each sample, three or five images with a scan size of 4 × 4 μm were collected in different regions with a scan rate of 0.3–0.5 Hz and with a resolution of 256 × 256 points. Surface roughness parameters, such as the average roughness (S_a) and the root mean square roughness (S_q), were calculated after slope corrections for the entire scan area (4 × 4 μm), according to the equations:

$$s_a = \frac{1}{MN} \sum_{k=0}^{M-1} \sum_{l=0}^{N-1} |z(x_k, y_l)|$$

$$s_q = \sqrt{\frac{1}{MN} \sum_{k=0}^{M-1} \sum_{l=0}^{N-1} (z(x_k, y_l))^2}$$

3. Results and discussion

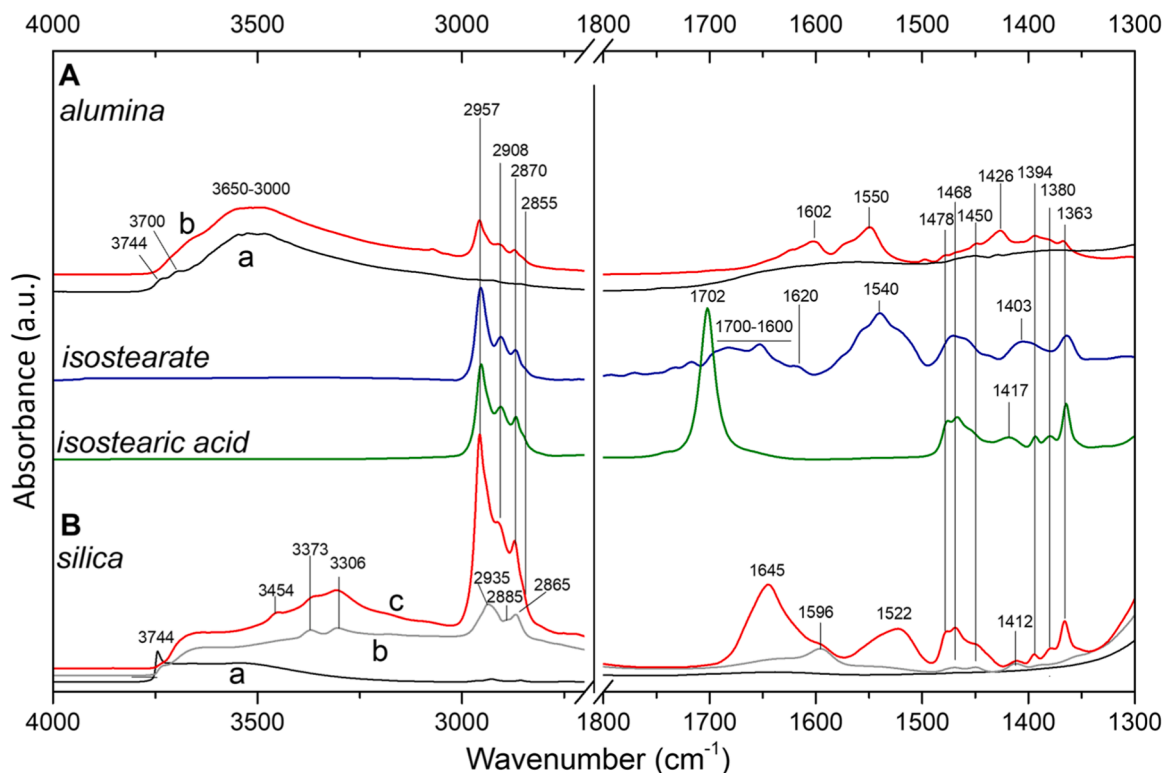### 3.1. Surface features of pristine and functionalized nanoparticles: quantitative aspect

The physico-chemical properties of the pristine, functionalized, and commercial hydrophobic silica and alumina materials used in the present work are reported in Table 1. Commercial materials (A300, AluC, AluC805, AR812) have well-defined properties as provided, which have been however checked in this work or elsewhere. In particular, the corresponding specific surface areas (SSAs) of the materials were calculated from the N$_2$ adsorption-desorption isotherms, while particle size was reported elsewhere, as detailed in Table 1. The pristine alumina (AluC) and commercial hydrophobic material (AluC805) of primary particles size of 13 nm are characterized by a SSA of 100 m^2 g^{-1}. This value is barely affected (91 m^2 g^{-1} for AluC-ISOST) after functionalization with ISOST. A300 and the commercial hydrophobic one (AR812) of primary particle size of 7 nm have higher SSAs of ca. 300 m^2 g^{-1} compared to the alumina samples. This value decreases to ~200 m^2 g^{-1} after functionalization with APTS and ISOST. On the other hand, A300 and AR812 clearly differ by the surface silanol groups density estimated to be 5.6 and 0.44 SiOH nm^{-2}, respectively. The density of the surface hydrophobic moieties for silica and alumina samples were estimated by TGA measurements (see Figs S1-S3 in the Supporting Information (SI)). Furthermore, the density of the surface amine groups on the functionalized silica sample (A300-APTS) of 1.2 NH$_2$ molec nm^{-2} was calculated by FTIR (see Fig. S4 in the SI) and confirmed by TGA measurements.

3.2. Insights at molecular level of functionalization of nanoparticles: FTIR studies

Information on chemical bonding of ISOST on alumina and silica nanoparticles was obtained by IR spectroscopy. Fig. 1 shows relevant spectra of pristine and functionalized nanoparticles taken after outgassing at b.t., ca. 323 K, in the IR cell, resulting in the complete desorption of water molecules initially adsorbed on the samples for silica and an incomplete one for alumina (see Fig. S5 in the SI). Moreover, the spectra of ISOST in the acid and isostearate form are also reported for comparison. For the sake of clarity and brevity, the detailed assignment of signals appearing in the whole set of spectra is reported in Table 2. For this reason, the references supporting the assignments in the text below will be no longer quoted.

Focusing on the spectra of ISOST in the acid and isostearate forms, signals due to —CH$_X$ stretching (ν, 3000–2800 cm^{-1}) and bending (δ, 1500–1350 cm^{-1}) modes appear almost equivalent in the two cases, whereas the main expected difference is in the features due to the functional group. In the case of —COOH, the peak at 1702 cm^{-1} is distinctive of the νC=O mode (in terms of group frequency), and the combination of the deformation δ mode of the —CH moiety in the α carboxylic group with the δ-COH one, results in the broad signal at 1417 cm^{-1}. Moving to the spectrum of the isostearate form, signals at 1540

Table 1

Physico-chemical properties of alumina and silica materials before and after functionalization along with corresponding commercial hydrophobic materials.

Al$_2$O$_3$	SSA$_{BET}$ (m^2 g^{-1})	Surface hydrophobic moieties density (molec nm^{-2})	Mean size of primary particles (nm)
AluC	100	–	13 [48]
AluC-ISOST	91	0.6	–
AluC805	100	3	13 [40]

SiO$_2$	SSA$_{BET}$ (m^2 g^{-1})	Surface silanol groups density (SiOH nm^{-2})	Surface amine groups density (-NH$_2$ molec nm^{-2})	Surface hydrophobic moieties density (molec nm^{-2})	Mean size of primary particles (nm)
A300	300	5.6	–	–	7 [49]
A300-APTS	200	5.2	1.2	0.7–1.7	–
A300-APTS-ISOST	196	–	–	0.4	–
AR812	260	0.44[48]	–	3.5 [50]	7 [40]

Fig. 1. IR spectra of alumina AluC (upper panel, A) and silica A300 (lower panel, B) materials in the pristine form and after functionalization with ISOST, all outgassed at b.t. (ca. 50 °C) in the IR cell. Alumina AluC: a) pristine form; b) after functionalization with ISOST. Silica A300: a) pristine form; b) after functionalization with APTS; c) after subsequent functionalization with ISOST. Spectra of ISOST in basic aqueous solution (isostearate) and in the pure liquid form (isostearic acid) are reported for comparison.

Table 2
List of major IR bands in Fig. 1 along with their assignments.

Bands positions (cm⁻¹) in the IR spectra of							Band Assignment
AluC	AluC-ISOST	Isostearate	Isostearic acid	A300	A300-APTS	A300-APTS-ISOST	
3737 and 3700				3744			νOH (isolated) [51]
3650–3000	3650–3000						νOH (H-bonded) [51]
				3700–3200	3700–3200	3700–3200	νOH (H-interacting) [51]
						3454	νNH (amide) [52]
					3373		ν_{asym}NH$_2$ [52]
					3306		ν_{sym}NH$_2$ [52]
	2957	2957	2957			2957	ν_{asym}CH$_3$ [52]
	2908	2908	2908	2935		2908	ν_{asym}CH$_2$ [52]
	2870	2870	2870	2885		2870	ν_{sym}CH$_3$ [52]
	2855	2855	2855	2865		2855	ν_{sym}CH$_2$ [52]
		1685–1675	1702				νC=O [53]
						1645	νCO (Amide I) [52]
	1620						δOH (water) [51]
1602							ν_{asym}COO⁻ (unidentate structure) [53]
					1596	1596	δNH$_2$ [52]
1550	1540						ν_{asym}COO⁻ (bridging structure) [53]
						1522	νCN + δNH (Amide II) [52]
1478			1478			1478	δCH$_2$ close to C-(CH$_3$)$_3$ [52]
1468	1468		1468		1468	1468	δ_{sym}CH$_3$ in C—CH$_3$ [52]
1450	1450		1450		1450	1450	δCH$_2$ [52]
1426	1403						ν_{sym}COO⁻ [53]
			1417				δCOH + δCH [52]
					1412	1412	δCH$_2$ in CH$_2$—CH [52]
1394	1394		1394			1394	δ_{sym}CH$_3$ in C-(CH$_3$)$_3$ [52]
1380	1380		1380			1380	δ_{sym}CH$_3$ in C—CH$_3$ [52]
1363	1363		1363			1363	δ_{sym}CH$_3$ in C-(CH$_3$)$_3$ [52]

and 1404 cm⁻¹ are assignable to the *asym* and *sym* νCOO⁻ modes, respectively, while the broad and complex features spread over the 1700–1600 cm⁻¹ range can be ascribed to the νC=O mode of undissociated carboxylic groups (in equilibrium with the deprotonated ones) [12] H-bonded with water molecules and/or interacting with Na⁺ cations introduced with the base. In both cases, the interaction results in a decrease of the νC=O frequency and the presence of a rich series of sub-bands that can be related to local heterogeneity in solvation of both

—COOH moieties and —COOH···Na$^+$ adducts.

3.2.1. ISOST on alumina AluC

The only IR features related to surface species present in the spectrum of alumina AluC outgassed at b.t. (Fig. 1, panel A, curve a) are a broad band spread over the 3650–3000 cm^{-1} range, due to the O—H stretching mode (νOH) of H-bonded surface hydroxy groups, and definitely weaker components at ca. 3700 and 3737 cm^{-1}, due to isolated surface OH groups. After functionalization with ISOST (Fig. 1, panel A, curve b), a depletion of the weak component at ca. 3737 cm^{-1} occurs, and a rich series of signals due to the organic molecules grafted on the surface appears. The set of signals in the 3000–2800 cm^{-1} range, due to —CH$_3$ and —CH$_2$ stretching modes, seems almost coincident with those in the spectra of ISOST in both acid and isostearate forms, in agreement with the slight sensitivity of these modes to the states of alkyl chains. At lower frequency, the δCH$_X$ pattern is less defined, because it is overlapped to a broad feature, with a better-defined component at 1426 cm^{-1}, assignable to the ν_{sym} mode of —COO$^-$ groups coordinated to surface Al^{3+} ions, with the ν_{asym} mode being responsible for the bimodal pattern in the 1650–1500 cm^{-1} range. Owing to the dependence of the ν_{asym}-ν_{sym} splitting of —COO$^-$ groups on their coordinative structure [53], the multiplicity of both ν_{asym} and ν_{sym} —COO$^-$ components indicate the occurrence of a variety of grafting structures. Nevertheless, the better definition of the component at 1426 cm^{-1} seems to mirror those at 1550 and 1602 cm^{-1}. Depending on the pairing (1602 and 1426 cm^{-1}, or 1550 and 1426 cm^{-1}, disambiguation not possible with the present data), the ν_{asym}-ν_{sym} splitting can be 176 or 124 cm^{-1}. Both values are close to 137 cm^{-1} obtained for isostearate in aqueous solution, suggesting the presence of carboxylate groups forming bridging complexes with surface Al^{3+} ions, in addition to other possible structures.

Finally, the presence of —COO$^-$ coordinated to Al^{3+} ions implies the transfer to surface basic oxygen atoms of protons from pristine —COOH groups. The resulting new surface OH groups should be responsible of the increase in intensity of the broad signal in the 3650–3000 cm^{-1} range, as well as of the depletion of the weak component at ca. 3737 cm^{-1}, because of their protonation (if basic), or by H-bonding with the newly formed surface hydroxy groups.

3.2.2. ISOST on silica A300

In the case of silica, the direct functionalization with ISOST, for instance via formation of surface ester linkages by condensation between surface silanols ≡SiOH and —COOH groups, resulted totally ineffective, thus these nanoparticles underwent a first functionalization with APTS, and then newly introduced -NH$_2$ groups were exploited for covalent bonding of ISOST by amide bonds, via conversion of —COOH groups in acyl chloride ones (see Materials and Methods).

The IR spectrum of bare A300 (Fig. 1, panel B, curve a) shows a peak at 3744 cm^{-1} due to the isolated/slightly interacting silanols and a broad band in the 3700–3200 cm^{-1} range, produced by silanols experiencing a mutual interaction; the stronger the interaction, the lower the corresponding νOH frequency. The functionalization with APTS (Fig. 1, panel B, curve b) resulted in an almost complete depletion of the peak at 3744 cm^{-1} and in the increase in intensity and widening towards further lower wavenumbers of the band due to interacting silanols. As far as quantitative aspects are concerned, functionalization with APTS results in a decrease of ca. 7 % of the signal due to ≡Si-OH in the ^{29}Si MAS SSNMR spectrum (see Fig. S6 in the SI).

Changes in the IR νOH pattern are accompanied by the appearance of a doublet at 3373 and 3306 cm^{-1}, due to ν_{asym} and ν_{sym} of -NH$_2$ groups, a pattern in the 3000–2800 cm^{-1} range typical of ν_{asym} and ν_{asym} of —CH$_2$ groups of the propyl chains and of —CH$_2$ and CH$_3$ groups of ethoxy moieties still present in a part of anchored APTS, as revealed by ^{13}C CPMAS SSNMR spectroscopy (see Fig. S7 in the SI). Moreover, a band at 1596 cm^{-1}, due to the δNH$_2$ mode, and the series of components in the 1500–1350 cm^{-1} range produced by δCH$_X$ modes are present. The successful formation of amide bonds in the subsequent functionalization step with ISOST (Fig. 1, panel B, curve c) is then witnessed by the appearance of intense bands at 1645 and 1522 cm^{-1}, in the typical ranges of νC=O and νCN + δNH mode of amides, and the component at 3454 cm^{-1}, due to the νNH mode of isolated amides, while the alkyl chains of ISOST produced the pattern in the 3000–2800 and 1500–1350 cm^{-1} ranges, in analogy with the other samples depicted in the figure.

The isolation of amide bonds results from the huge steric hindrance of the iperbranched structure of ISOST. Consequently, the consumption of —NH$_2$ surface groups is quite limited, as indicated by the slight decrease in intensity of the δNH$_2$ band at 1596 cm^{-1}, and some fading of the NH$_2$ ν_{asym} and ν_{sym} doublet at 3373 and 3306 cm^{-1}. This latter one appears overlapped to a slightly more intense broad band due to interacting silanols, resulting from the perturbation of these groups by the newly anchored molecules (also responsible by the complete depletion of the signal at 3744 cm^{-1}).

3.3. Interaction of pristine and functionalized nanoparticles with water vapor

The second target of the work was the investigation of the effect of surface functionalization on its behavior towards water vapor, by measuring amount, spectroscopic and energetic features of adsorbed H$_2$O molecules. As for the amount, the number of water molecules per nm^2 was calculated, combining microgravimetric data (μg of adsorbed water per mg of sample) with SSA$_{BET}$ values, thus the adsorption capability will be referred to as specific capability to adsorb water. For the sake of comparison, commercial hydrophobic alumina (AluC805) and silica (AR812) nanoparticles were also considered.

3.3.1. Quantitative aspects: microgravimetry

Fig. 2 shows the amount of water molecules adsorbed per nm^2 by samples in contact with water vapor at 298 K and 20 mbar, i.e. the maximum pressure reached during microgravimetric measurements for all samples. The complete adsorption isotherms are reported in Figs S8 and S9 in the SI. Bare AluC shows the highest specific capability to adsorb water (11 H$_2$O molec nm^{-2}), that is decreased by only ca. 40 % by functionalization with ISOST (6.5 H$_2$O molec nm^{-2}), being ca. two times higher of that showed by commercial AluC805 (3.4 H$_2$O molec nm^{-2}). Passing to silica, bare A300 appears capable to adsorb less water molecules per surface unit (5.2 H$_2$O molec nm^{-2}) than bare AluC, whilst the capability slightly increased after functionalization with APTS, (6.2 H$_2$O molec nm^{-2}), likely because of the replacement of some isolated silanols (unable to adsorb water at r.t.) [51,54,55] with moieties terminated by the -NH$_2$ group, more effective in the interaction with
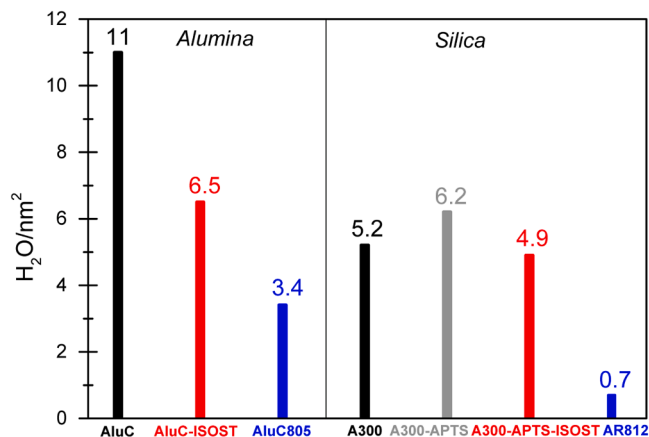

Fig. 2. Microgravimetry analysis on alumina (AluC, AluC-ISOST, AluC805) and silica (A300, A300-APTS, A300-APTS-ISOST, AR812) materials. The number of water molecules adsorbed per nm^2 is reported on top of the bars.

H$_2$O molecules [56]. The subsequent functionalization with ISOST resulted in a quite limited decrease (ca. 10 %) of the specific capability to adsorb water (4.9 H$_2$O molec nm^{-2}), definitely larger than the very poor capability shown by commercial AR812 (0.7 H$_2$O molec nm^{-2}).

As a whole, the surface functionalization with ISOST had a limited impact (very limited, in the case of silica) on the specific capability to adsorb water vapor, definitely lower than what resulted from the functionalization with non-highly branched alkyl moieties, as those present in commercial hydrophobic nanoparticles. Actually, ISOST molecules used in this work are made of two main sub-chains of 4 and 5 C atoms linked to the C atom in α position with respect to the carboxyl group exploited for linking to the surface (Fig. S10). The conformational dynamics of such a structure can leave room to water molecules in vapor phase to come into contact with surface sites (Al^{3+} centres, Si-OH, -NH$_2$) not involved in the linking to the surface of ISOST molecules. Moreover, in the case of silica, moieties resulting from the grafting of APTS act also as a spacer between the surface of nanoparticles and covalently bonded ISOST, and this can well explain the very limited decrease in specific capability to adsorb water observed by passing from A300-APTS to A300-APTS-ISOST.

Such a possibility appears to be more limited in the case of commercial alumina-based AluC805, functionalized with quite long linear alkyl chains (C8), but attaining a definitely higher surface density (3 units per nm^2 vs 0.6 units per nm^2 for A300-APTS-ISOST, see Table 1).

The definitely smaller molecular size of hexamethyldisilazane (Fig. S11) used for the surface functionalization of commercial silica-based AR812 allowed for the attainment of an even higher surface density (3.5 units per nm^2), with a consequent larger consumption of surface silanols, and this might be the main reason of the poor capability to adsorb water shown by this material.

3.3.2. States of adsorbed water: near-IR spectroscopy

In order to assess possible effects of the presence of ISOST on the states of adsorbed water molecules, NIR spectra of pristine and functionalized nanoparticles in contact with water vapor at decreasing pressure were collected (Fig. 3). For the sake of completeness, equivalent data for commercial hydrophobic nanoparticles were obtained (see Figs S12 and S13 in the SI). The focus was on the pattern due to the $\nu_{asym}+ \delta$ combination mode of adsorbed molecules, falling in a range (5500–4600 cm^{-1}) free of contributions from surface hydroxy groups, as conversely occurs in the νOH range in the mid-IR. The analysis of such pattern is highly effective for obtaining information on the state of water molecules, because the higher are the number and strength of H-bonding donations experienced by water molecules, the broader and lower in frequency the resulting $\nu_{asym}+ \delta$ feature [51].

Moreover, the state of adsorbed water molecules depends on the surface coverage. As reported in the previous section, the maximum water coverage decreases when passing from AluC to AluC-ISOST and from A300-APTS to A300-APTS-ISOST ($\approx$ A300) (Fig. 2). Hence, for AluC and A300-APTS, only spectra taken at surface coverages similar to those attained on the corresponding functionalized materials (and A300, for the silica-based set of nanoparticles) were considered for comparison. The full series of spectra collected for AluC and A300-APTS, including those at higher water surface coverage, are shown in Fig. S14 in the SI.

The $\nu_{asym}+ \delta$ patterns obtained for H$_2$O molecules adsorbed on AluC and AluC-ISOST are shown in Fig. 3, panels A and B. In both of them, the spectrum of bulk water (dotted line) is also reported for comparison. Starting with bare AluC (Fig. 3, panel A), the spectrum at the maximum considered water coverage (Fig. 3, panel A, curve a) shows a main component at 5170 cm^{-1}, accompanied with a shoulder at 5280 cm^{-1}. The main component appears located at lower frequency with respect to the $\nu_{asym}+ \delta$ signal of bulk water (at 5180 cm^{-1}), and shows a wider
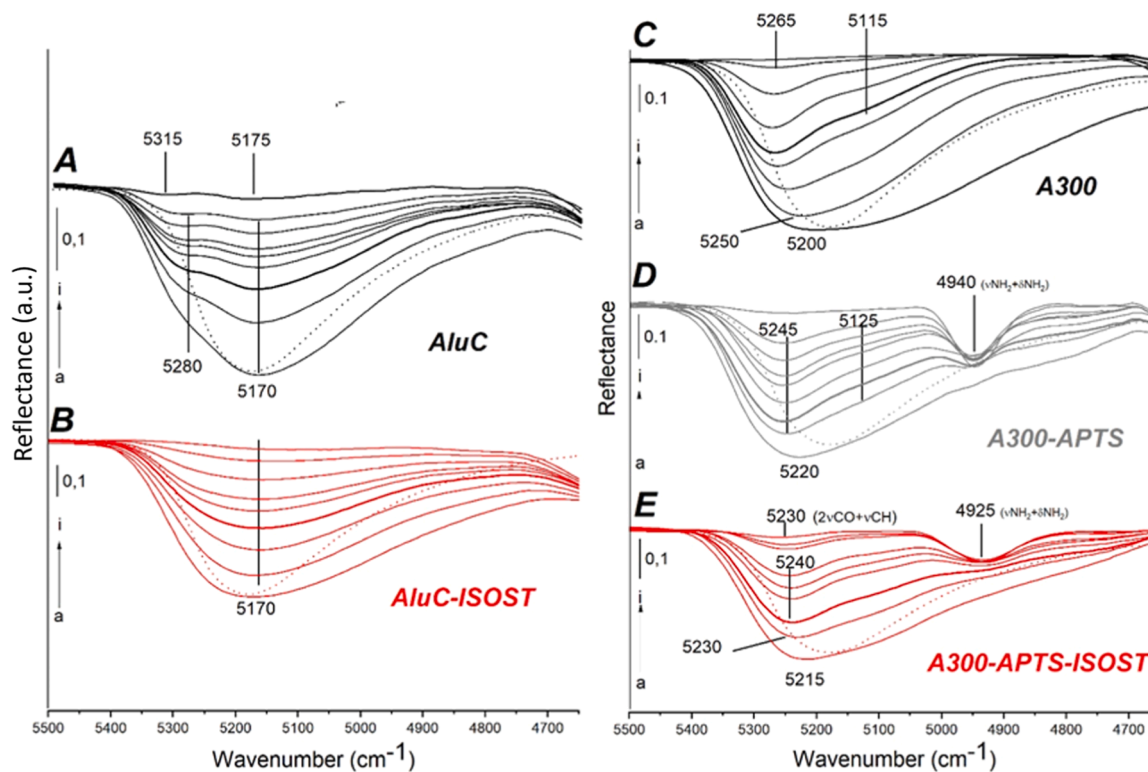
Fig. 3. NIR spectra of water adsorbed over alumina (left) and silica (right) materials: AluC (panel A), AluC-ISOST (panel B), A300 (panel C), A300-APTS (panel D), A300-APTS-ISOST (panel E). The spectra are recorded in equilibrium with water vapor pressure (a curves) followed by stepwise outgassing (b-h curves) until invariance of the spectra (i curves). The detailed description of the spectra in the wider near-IR region (8000–4000 cm^{-1}) is reported in Figs S15 and S16 in the SI. The spectrum of liquid water is reported as dotted line, for comparison.

asymmetric broadening towards the low-frequency side. Both features indicated that most part of adsorbed water molecules are experiencing H-bonding interactions (as donors) slightly stronger than what is occurring among H_2O molecules in liquid water. Conversely, the shoulder at 5280 cm^{-1} is due to molecules at the actual interface between the adsorbed and the vapor phase, expected to point at least one -OH towards the exterior, also indicated as "dangling" —OH moieties [56,57]. This shoulder progressively gains in relative intensity by decreasing the water coverage, in agreement with an increase of the relative amount of interfacial water molecules with respect to the total amount of adsorbed ones. After outgassing at r.t. (Fig. 3, panel A, curve i), only very weak signals at 5315 cm^{-1} and 5175 cm^{-1} remain, due to water molecules coordinated to surface Al^{3+} sites with a high coordinative unsaturation level (see Fig. S5 and related comments). Apparently, these molecules are oriented with one OH pointing outward (signal at higher frequency) and the other interacting via H-bonding with a surface O atom (signal at lower frequency).

The presence of isostearic moieties has a non-negligible impact on the states of water adsorbed on AluC-ISOST (Fig. 3, panel B). The main component of the $\nu_{asym}+\delta$ signal of adsorbed H_2O still shows the same position, whilst it appears significantly broader on the lower-frequency side than in the previous case, as inferred by the comparison with the signal of bulk water. This behavior indicates the reinforcement of H-bonds involving some adsorbed H_2O molecules. Such behavior might result from the interaction of these molecules with the oxygen atoms of the carboxylate groups anchoring ISOST molecules to the alumina surface. Interestingly, the shoulder at high frequency due to dangling —OH groups pointing towards the exterior is almost absent. A similar behavior was observed in the mid-IR for H_2O molecules at a liquid water/hexene interface, where the component to interfacial "dangling" —OH groups appeared significantly less intense with respect to the corresponding signal observed for liquid water/water vapor or CCl$_4$ interfaces [57]. Thus, the significant decrease in the intensity of the high-frequency shoulder can be used to monitor the occurrence of an actual interaction between adsorbed water molecules and overlying alkyl branches of anchored ISOST molecules. Similar spectral features and evolution by decreasing the water coverage were observed for commercial AluC805 (see Fig. S12 in the SI).

A second, expected effect is the complete desorption of water molecules by outgassing at r.t., indicating that surface Al^{3+} sites with a higher coordinative unsaturation level are among those involved in the coordination of carboxylate groups allowing for the anchoring of ISOST molecules to the surface.

Moving to the silica-based set of nanoparticles (Fig. 3, panels C–E), the $\nu_{asym}+\delta$ signal of water adsorbed on A300 at maximum surface coverage shows a squat reflectance minimum at 5200 cm^{-1} (Fig. 3, panel C). The spectral evolution at decreasing coverages indicates that such shape results from the overlapping of a broad component widely asymmetric on the low-frequency side, progressively evolving into a shoulder at 5155 cm^{-1} and a narrower component progressively becoming the dominant one, and shifting from 5250 to 5265 cm^{-1}. In comparison with the case of water on AluC (Fig. 3, panel A), the relative intensity of these high- and low-frequency components appears reversed, indicating that a larger fraction of H_2O adsorbed on A300 should point one or both -OH moieties (responsible for the high-frequency component) towards the exterior. Moreover, the downshift of the low-frequency component indicates that the remaining part of the -OH moieties are involved in stronger H-bonds.

In the case of A300-APTS (Fig. 3, panel D), the presence of grafted APTS increases the complexity of the interaction with water, because -NH$_2$ groups can act as adsorbing sites for H_2O molecules, and water adsorbed on remaining surface silanols can also interact with the apolar moieties of APTS, namely the propyl chain and the ethoxy groups that resisted hydrolysis (see Fig. S7 in the SI). The role of -NH$_2$ groups as adsorbing sites is clearly indicated by the behavior of the signal at 4940 cm^{-1} due to their $\nu_{asym}+\delta$ mode, progressively gaining in definition and intensity as the water coverage is decreased, clearly indicating that they are involved in the interaction with H_2O molecules.

Focusing on the spectral pattern due to adsorbed water, the low-frequency component due to H-bonded -OH moieties appears even less pronounced and slightly upshifted with respect to the case of H_2O molecules on bare A300, indicating some weakening of H-bonding. The high-frequency component due to —OH moieties pointing toward the exterior is conversely downshifted by ca. 20 cm^{-1}. On the basis of the downshift of ca. 30 cm^{-1} observed in the mid-IR for interfacial —OH of water when passing from the liquid/vapor interface to the liquid/CCl$_4$ and liquid/hexane ones [57], such a change in position might result from the interaction with the apolar moieties of grafted APTS.

The additional presence of ISOST chains has a limited impact on the spectral profile of water adsorbed on A300-APTS-ISOST (Fig. 3, panel E), likely because of the similarity of their interaction with underlying H_2O molecules of the latter with the apolar moieties of anchored APTS. Indeed, the main effect is a further 5 cm^{-1} downshift of the H_2O $\nu_{asym}+\delta$ component due to -OH moieties pointing toward the exterior, in agreement with the increase of the apolar character of the interface overlying adsorbed water molecules. Notably, also —NH$_2$ groups of anchored APTS that were not consumed in the conjugation with ISOST molecules seem to experience an interaction with ISOST chains similar to that proposed for water, because the —NH$_2$ $\nu_{asym}+\delta$ appears now 10 cm^{-1} lower in frequency than in the case of A300-APTS.

Finally, the signal at 5230 cm^{-1} remaining after water outgassing is due to the overtone/combination mode of $2\nu CO + \nu CH$ of the ISOST linked to the surface.

3.3.3. Energetics of water molecules adsorption: microcalorimetry

The limited impact of the presence of long and branched alkyl chains on water adsorption from the vapor phase by functionalized alumina-based and silica-based nanoparticles, was confirmed by measuring the adsorption enthalpy ($-\Delta_{ads}H$) by introducing H_2O vapor at increasing pressure (Fig. 4). As reported in the Materials and Methods section, the maximum pressure was 10 mbar, thus in most cases the maximum amount of adsorbed water molecules was lower than that obtained in the microgravimetric measurements, allowing for an increase of the vapor pressure to 22 mbar. An additional piece of information relevant for the evaluation of water adsorption enthalpy data is that they are usually compared with the latent enthalpy of liquefaction of water ($-\Delta_{liq}H(H_2O)$) = 44 kJ mol^{-1}, dotted line in both panels). Water adsorption enthalpy values higher or lower than $-\Delta_{liq}H(H_2O)$ are usually associated with a hydrophilic of hydrophobic character of adsorbing surfaces, respectively [58]. On such a basis, it can be stated that, in the range of water surface coverage attained, the interaction of H_2O molecules with bare AluC (Fig. 4, panel A, curve a) has always a hydrophilic character, progressively decreasing by increasing water coverage, because the first doses of H_2O molecules are preferentially adsorbed on stronger adsorbing sites [58]. Basically, the same statement holds for water on AluC-ISOST and commercial alumina-based AluC805, although $-\Delta_{ads}H$ measured at the highest water uptake attained are slightly lower than $-\Delta_{liq}H(H_2O)$ (Fig. 4, panel A, curve b and c, respectively). Notably, the order of the highest water uptake for these three materials follows the one found by contact with water vapor at a higher pressure in microgravimetric measurements (Fig. 2).

The energetics of water adsorption on silica A300-based nanoparticles (Fig. 4, panel B) appears even less dependent on the surface features, with similar water adsorption enthalpy values for bare A300, A300-APTS, and A300-APTS-ISOST (Fig. 4, panel B, curves a–c, in the order). With respect to the alumina-based materials, the whole sets of values are lower, because surface silanols and -NH$_2$ groups are weaker adsorbing sites than surface Al^{3+}ions, and at the highest water uptake attained, all three A300-based nanoparticles showed a slightly hydrophobic character. Moreover, water uptake by these three types of nanoparticles becomes progressively more similar as water coverage increases, in agreement with the limited difference in water uptake by
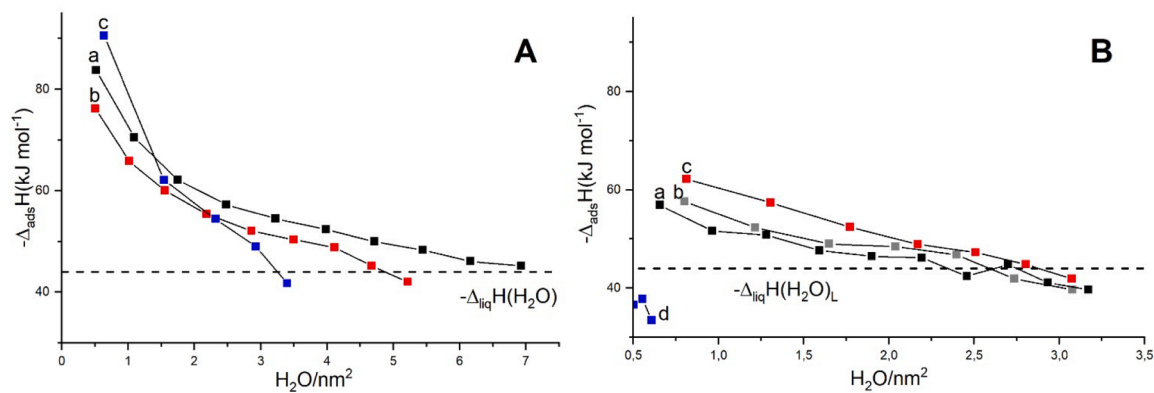
Fig. 4. Adsorption enthalpy versus uptake of H_2O molecules on alumina-based (panel A) and silica-based (panel B) nanoparticles. Panel A a) AluC, b) AluC-ISOST, c) AluC805. Panel B: a) A300, b) A300-APTS, c) A300-APTS-ISOST, d) AR812. All materials were pre-outgassed at 303 K. Dotted line: latent enthalpy of liquefaction of water.

contact with H_2O vapor at 22 mbar in microgravimetric measurements (Fig. 2). Still in agreement with those data, water uptake by commercial silica-based AR812 appears definitely limited, resulting from adsorption enthalpy values definitely lower than $-\Delta_{liq}H(H_2O)$ (Fig. 4, panel B, curve d).

3.4. States of alkyl chains of ISOST anchored on alumina and silica nanoparticles

To complete the characterization at a molecular level of the surfaces "seen" by liquid water droplets used in contact angle measurements (see next subsection), the states of alkyl chains of ISOST molecules anchored on AluC and A300-APTS were investigated by ^{13}C CPMAS SSNMR spectroscopy of AluC-ISOST and A300-APTS-ISOST exposed to air. The results are shown in Fig. 5.

The highest-frequency region witnesses the different interaction of ISOST with alumina and silica materials: the peak at 182 ppm in the AluC-ISOST (Fig. 5, curve a) refers to a carboxylic group, and combining the information with IR measurements, it is possible to assign the peak to carboxylate species.

The signal at 177 ppm, for A300-APTS-ISOST (Fig. 5, curve b), is typical of an amidic compound, and this confirms the presence of Amide I and Amide II bands in the mid-IR spectra.

Both spectra contain typical peaks of a long aliphatic chain; in particular, peaks that fall at lower chemical shifts (60–20 ppm) are assigned to the aliphatic chain of ISOST. Some peaks (43.0 ppm, 22.3 ppm and 9.5 ppm, labelled with ## and #) in A300-APTS-ISOST are "affected" by the presence of APTS; however, there are regions where only signals referring to the alkyl chains of ISOST fall (~50 and 30 ppm). The intensity and the shape of these peaks in the two spectra slightly change, due to the different surface density (0.6 and 0.3 molec nm^{-2} for alumina and silica, respectively) and the different orientation of the
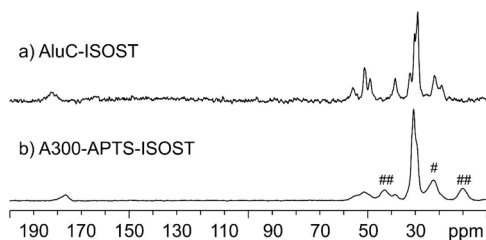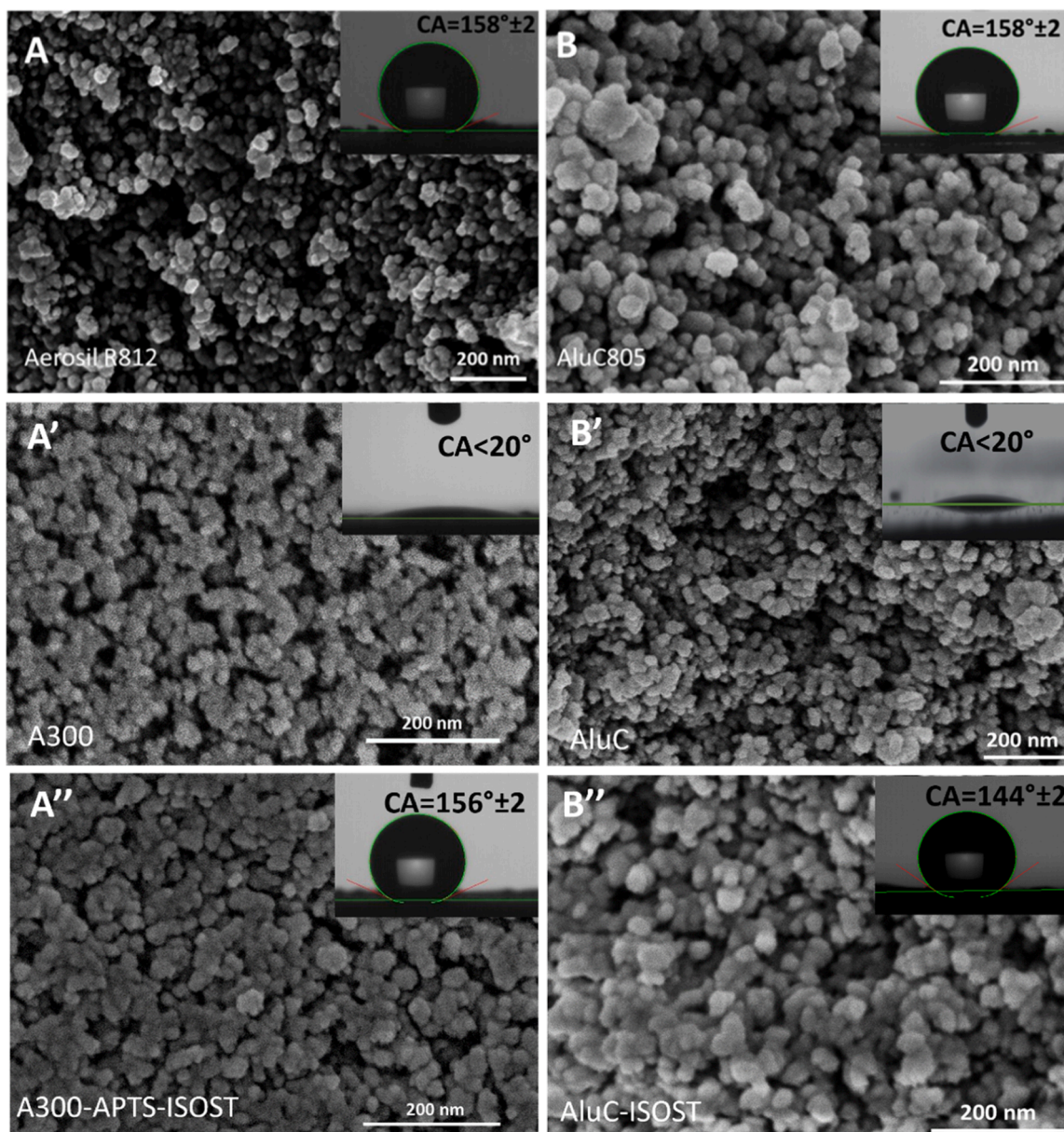
molecule on the surface.

3.5. Behavior towards liquid water at macroscopic level: contact angle measurements

In the previous part of this work, the study of the molecular behavior of the materials towards water was carried out, witnessing a good capability to adsorb water vapor even for modified materials with hydrophobic molecules. Nevertheless, another aspect to investigate is the macroscopic behavior of these materials towards water droplets, and consequently the study of their morphology through electron microscopy. This latter aspect results to be very attractive, in particular for a specific characteristic required for hydrophobic materials. Although the presence of non-polar molecules exposed on the surface (e.g. hydrocarbons) reflects the intrinsic hydrophobic chemistry of the material, another requirement to enhance the water-repellence is the surface roughness that allows reaching superhydrophobicity ($\theta > 150°$) [40]. The specific construction of micro-nano hierarchical microstructures on the surface combined with a low surface energy is inspired by nature; these characteristics are intrinsically present on several primary part of plants [12] and in particular in the Lotus leaf, from which the "Lotus effect" takes its name [10]. This kind of topography forms air gaps between microstructures that are totally hydrophobic [59]. Several works on the preparation of superhydrophobic materials [40,60,61] are based on the relation between superhydrophobicity and the presence of microstructures on the surface. The investigation of the hydrophobicity through contact angle analysis and SEM images is typically carried out on samples that are sprayed on a surface, as films or hydrophobic coatings.

In this work, the samples were analyzed as a self-supporting pellet, in which the powders of silica nanoparticles are pressed at ca. 1 ton (see Materials and Methods). This kind of procedure creates a flat and homogeneous surface, totally different from the texture of a sprayed coating.

In Fig. 6, the FESEM images for silica samples show that the surface morphology of the modified silica nanoparticles with ISOST (A300-APTS-ISOST, Fig. 6, panel A") does not present significant changes when compared to the unmodified commercial silica (A300, Fig. 6, panel A'). In both cases typical aggregates of silica are clearly visible, but no hierarchical microstructures that could entrap a thin air layer on the surface seem to appear. The same feature was observed for alumina materials (AluC and AluC-ISOST, Fig. 6, panels B' and B" respectively). The FESEM images for the hydrophobic commercial silica (AR812, Fig. 6, panel A) and alumina (AluC805, Fig. 6, panel B) materials are reported for comparison.

The measurements of the static contact angle on the same self-supporting pellets in Fig. 6 show an unexpected result. For A300-

Fig. 5. ^{13}C (100.63 MHz) CPMAS SSNMR spectra of a) AluC-ISOST and b) A300-APTS-ISOST exposed to air, acquired at room temperature at a spinning frequency of 12 kHz. Signals labelled with (##) and (#) in the spectrum of A300-APTS-ISOST are due to or contributed by the propyl chain of APTS, respectively.

Fig. 6. FESEM images for silica: (A) AR812, (A') A300, (A") A300-APTS-ISOST; and alumina samples: (B) AluC805, (B') AluC, and (B") AluC-ISOST. Insets report the corresponding contact angles.

APTS-ISOST (Fig. 6, panel A"), the value of contact angle ($\theta = 156°$) is greater than $150°$ (the limit value to consider a material as super-hydrophobic) even if no microstructures are visible in FESEM images. The presence of the highly branched carbon chains of ISOST on the surface of silica nanoparticles allows obtaining a superhydrophobic surface, compared to the hydrophilic behavior of the unmodified silica A300 nanoparticles ($\theta < 20°$, Fig. 6, panel A'). Moreover, although the hydrophobic commercial materials AR812 and AluC805 present the expected high contact angles, they still show similar levels of micro-nano hierarchical microstructure on the surface, as shown in Fig. 6, panels A and B, respectively.

The increase of the contact angle value for AluC-ISOST (Fig. 6, panel B"), compared to the bare alumina (Fig. 6, panel B'), does not lead to a superhydrophobic level witnessing the different orientations of the molecules on the surface of alumina or silica (see SSNMR studies) that can affect the wettability towards water droplets.

Finally, AFM measurements were carried out on the silica sample, to investigate their surface roughness, which could affect their

macroscopic behavior towards water. Representative AFM images of AR812, A300-APTS-ISOST, and A300 are shown in Fig. 7, while the areal roughness parameters (average roughness: Sa; root mean square roughness: Sq) are summarized in Table 3. Sa and Sq values were obtained from 3 to 5 scans performed on pelletized nanopowders over a scan area of 4×4 μm. Interestingly, these data reveal that the Sa and Sq values of the three samples are very similar, indicating the reproducibility of the method used to obtain the pellets. Furthermore, based on the roughness values, both Sa and Sq, we can conclude that the static contact angle measurements (AR812 $\cong$ A300-APTS-ISOST $>>$ A300) depend on the surface characteristics (i.e. functional groups) of the nanoparticles and not on the roughness of their surfaces.

4. Conclusions

The development of new sustainable processes for waterproofing purposes in industrial production of various consumer products has recently been on the top of research interests. In the present work, we
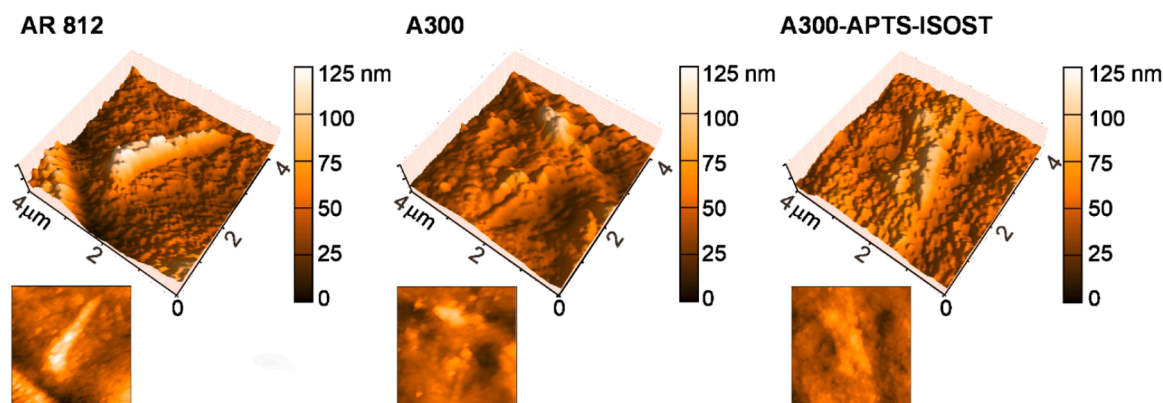
Fig. 7. Representative 3D and topographic AFM images of: AR 812, A300 and A300-APTS-ISOST.

Table 3
Areal roughness parameters, as obtained by 4×4 µm AFM scans.

Sample	Area Average roughness*, Sa (nm)	Root mean square roughness**, Sq (nm)
AR812	13,7 ± 4,9	18,6 ± 5,6
A300-APTS-ISOST	13,8 ± 2,7	17,4 ± 3,2
A300	13,6 ± 3,2	18,2 ± 4,3

studied the use of nanomaterials (e.g. silica) as water proofing agents for the substitution of the conventionally applied perfluoroalkyl substances (PFAs) in hydrophobic coatings. The novelty of this work lies first in the functionalization of silica nanoparticles with isostearic acid, a fluorine-free, biodegradable, cheap and non-toxic molecule constituted of highly branched alkyl chains and which positively affects the hydrophobicity of the surface. Isostearic acid has been used instead of the hexamethyldi-silazane employed for the functionalization of commercial silica as the latter has shown a remarkable toxicity, environmental persistence, and high cost [62]. The experimental research method adopted for silica nanoparticles functionalization results in the formation of a super-hydrophobic surface characterized by a contact angle higher than 150°. Noticeably, alumina nanoparticles functionalized with isostearic acid following a literature procedure do not show the same super-hydrophobic properties (contact angle 144° ± 2°), notwithstanding the higher water vapor uptake and adsorption enthalpy. The study of the augmented functionality of nanomaterials using various characterization techniques at the micro- and macroscopic scale evidences the possibility to reach an ultimate level of hydrophobicity without forming micro-nano hierarchical structures (known as "Lotus effect"). Furthermore, the characterization of the functionalized surface shows that a material with a contact angle higher than 150° can adsorb water vapor, revealing that the macroscopic behavior of such a surface towards water droplets can be different from the molecular behavior towards water vapor. The water adsorption capacity depends on the possibility of water vapor molecules to reach the parts of the surface not covered with hydrophobic moieties and it seems to be independent from the capacity of the hydrophobic chemical surface features to protect the surface from a macroscopic object such as water droplets. The results obtained in the present work represent an innovation in the field of sustainable production of hydrophobic coatings, given that no relevant studies of similar effect have been found up to now.

Author statement

During the preparation of this work the authors did not use generative AI and AI-assisted technologies in the writing process.

CRediT authorship contribution statement

Erica Rebba: Writing – original draft, Investigation, Formal analysis, Data curation. **Pavlo Ivanchenko:** Writing – original draft, Data curation. **Simone Bordignon:** Writing – review & editing, Investigation, Formal analysis, Data curation. **Ola El Samrout:** Writing – original draft. **Michele R. Chierotti:** Supervision, Methodology. **Federico Cesano:** Writing – original draft, Investigation, Formal analysis, Data curation. **Gloria Berlier:** Writing – review & editing, Supervision.

Declaration of competing interest

The authors declare that they have no known competing financial interests or personal relationships that could have appeared to influence the work reported in this paper.

Data availability

Data will be made available on request.

Supplementary materials

Supplementary material associated with this article can be found, in the online version, at doi:10.1016/j.surfin.2024.104535.

References

[1] Z. Wang, Y. Ren, F. Wu, G. Qu, X. Chen, Y. Yang, J. Wang, P. Lu, Advances in the research of carbon-, silicon-, and polymer-based superhydrophobic nanomaterials: synthesis and potential application, Adv. Colloid Interface Sci. (2023) 102932.
[2] H. Zhang, Z. Guo, Recent advances in self-healing superhydrophobic coatings, Nano Today 51 (2023) 101933.
[3] M. Ruzi, N. Celik, M.S. Onses, Superhydrophobic coatings for food packaging applications: a review, Food Packag. Shelf Life 32 (2022) 100823.

[4] Y. Ai, J. Zhang, F. Zhao, B. Zeng, Hydrophobic coating of polyaniline-poly (propylene oxide) copolymer for direct immersion solid phase microextraction of carbamate pesticides, J. Chromatogr. A 1407 (2015) 52–57.

[5] D. Ahmad, I. van den Boogaert, J. Miller, R. Presswell, H. Jouhara, Hydrophilic and hydrophobic materials and their applications, Energy Sources Part A Recover. Util. Environ. Eff. 40 (2018) 2686–2725.

[6] X. Yu, M. Zhang, H. Chen, Superhydrophobic anticorrosion coating with active protection effect: graphene oxide-loaded inorganic/organic corrosion inhibitor for magnesium alloys, Surf. Coatings Technol. (2024) 130586.

[7] J. Wei, X. Wei, M. Hou, J. Wang, Fluorine-free photothermal superhydrophobic copper oxide micro-/nanostructured coatings for anti-icing/de-icing applications, ACS Appl. Nano Mater. 6 (2023) 9928–9938.

[8] S. Xu, B. Shi, A green and sustainable strategy for leather manufacturing: endow dehydrated hide with consistent and durable hydrophobicity, J. Clean. Prod. 383 (2023) 135526.

[9] R.M. Ma, M. Hill, Superhydrophobic surfaces, Curr. Opin. Colloid Interface Sci. 11 (2006) 193–202.

[10] A. Marmur, The lotus effect: superhydrophobicity and metastability, Langmuir 20 (2004) 3517–3519.

[11] S. Cheng, S.S. Latthe, K. Nakata, R. Xing, S. Liu, A. Fujishima, Recent advancements in design, development and demands of photothermal superhydrophobic materials, Mater. Today Chem. 35 (2024) 101868.

[12] W.N.W. Barthlott, C.N.W. Neinhuis, Purity of the sacred lotus, or escape from contamination in biological surfaces, Planta 202 (1997) 1–8.

[13] D. Wang, N. Tang, L. Tong, W. Xiong, Fabrication of robust and scalable superhydrophobic surfaces and investigation of their anti-icing properties, Mater. Des. 156 (2018) 320–328.

[14] Z. Wang, W. Yang, F. Sun, P. Zhang, Y. He, X. Wang, D. Luo, W. Ma, G.-C. Sergio, Construction of a superhydrophobic coating using triethoxyvinylsilane-modified silica nanoparticles, Surf. Eng. 35 (2018) 418–425.

[15] M. Li, X.M. Reinhoudt, D. Crego-Calama, What do we need for a superhydrophobic surface? A review on the recent progress in the preparation of superhydrophobic surfaces, Chem Soc Rev 36 (2007) 1350–1368.

[16] D. Kotthoff, M. Müller, J. Jürling, H. Schlummer, M. Fiedler, Perfluoroalkyl and polyfluoroalkyl substances in consumer products, Environ. Sci. Pollut. Res. 22 (2015) 14546–14559.

[17] T.O.V. Stoiber, S. Evans, O.V. Naidenko, Disposal of products and materials containing per- and polyfluoroalkyl substances (PFAS): a cyclical problem, Chemosphere (2020) 127659.

[18] E. Kissa, No Title. Fluorinated Surfactants and Repellents, 2nd ed., Taylor & Francis, 2001.

[19] J. Ma, J. Zhang, X. Bao, Y. Liu, A facile spraying method for fabricating superhydrophobic leather coating, Colloids Surf. A Physicochem. Eng. Asp. 472 (2015) 21–25.

[20] T. Zhou, H. Niu, H. Gestos, A. Lin, Robust, self-healing superamphiphobic fabrics prepared by two-step coating of fluoro-containing polymer, fluoroalkyl silane, and modified silica nanoparticles, Adv. Funct. Mater. 23 (2013) 1664–1670.

[21] L. Xu, R.G. Karunakaran, J.R.G. Guo, S. Yang, Transparent, superhydrophobic surfaces from one-step spin coating of hydrophobic nanoparticles, ACS Appl. Mater. Interfaces 4 (2012) 1118–1125.

[22] F.-L. Tang, W. Huang, Y. Meng, W. Qing, Synthesis of fluorinated hyperbranched polymers capable as highly hydrophobic and oleophobic coating materials, Eur. Polym. J. 46 (2010) 506–518.

[23] H. Tian, Y. Yao, Y. Chang, S. Zhao, Z. Zhao, Y. Yuan, X. Wu, F. Sun, Occurrence and phase distribution of neutral and ionizable per- and polyfluoroalkyl substances (PFASs) in the atmosphere and plant leaves around landfills: a case study in Tianjin, China, Environ. Sci. Technol. 52 (2018) 1301–1310.

[24] R.J. Letcher, S.R.J. Chu, S.-A. Smyth, Side-chain fluorinated polymer surfactants in biosolids from wastewater treatment plants, J. Hazard. Mater. 388 (2020) 122044.

[25] P. Manea, S. Salmaso, L. Lorenzoni, G. Mazzucato, M. Russo, F. Mantoan, D. Martuzzi, M. Fletcher, T. Facchin, Exposure to PFAS and small for gestational age new-borns: a birth records study in Veneto Region (Italy), Environ. Res. 184 (2020) 109282.

[26] P. Mastrantonio, M. Bai, E. Uccelli, R. Cordiano, V. Screpanti, A. Crosignani, Drinking water contamination from perfluoroalkyl substances (PFAS): an ecological mortality study in the Veneto Region, Italy, Eur. J. Public Health 28 (2018) 180–185.

[27] H. Ye, H. Zhu, L. Li, W. Liu, H. Chen, Constructing fluorine-free and cost-effective superhydrophobic surface with normal-alcohol-modified hydrophobic SiO2 nanoparticles, ACS Appl. Mater. Interfaces 9 (2016) 858–867.

[28] J. Li, J. Wan, H. Ye, Y. Zhou, H. Chen, One-step process to fabrication of transparent superhydrophobic SiO2 paper, Appl. Surf. Sci. 261 (2012) 470–472.

[29] C. Morterra, G. Magnacca, A case study: surface chemistry and surface structure of catalytic aluminas, as studied by vibrational spectroscopy of adsorbed species, Catal. Today 27 (1996) 497–532.

[30] G. Lei, Y.G.C. Zheng, Y. Cao, L.Y.N. Shen, S.L.J. Wang, S.S.P. Liang, Y.S.P. Zhan, L. S.P. Jiang, Deactivation mechanism of COS hydrolysis over potassium modified alumina, Acta Phys.-Chim. Sin 39 (2023) 2210038.

[31] R. Réocreux, É. Girel, P. Clabaut, A. Tuel, M. Besson, A. Chaumonnot, P. Sautet, C. Michel, Reactivity of shape-controlled crystals and metadynamics simulations locate the weak spots of alumina in water, Nat. Commun. 10 (2019) 3139.

[32] L.T. Zhuravlev, The surface chemistry of amorphous silica. Zhuravlev model, Colloids Surf. A Physicochem. Eng. Asp. 173 (2000) 1–38, https://doi.org/10.1016/S0927-7757(00)00556-2.

[33] O.E. Samrout, G.O.E. Berlier, J.F.O.E. Lambert, Amino acid polymerization on silica surfaces, Chemplus chem (2024) e202300642.

[34] V. Bolis, B. Fubini, L. Marchese, G. Martra, D. Costa, Hydrophilic and hydrophobic sites on dehydrated crystalline and amorphous silicas, J. Chem. Soc. Faraday Trans. 87 (1991) 497–505, https://doi.org/10.1039/FT9918700497.

[35] V. Bolis, A. Cavenago, B. Fubini, Surface heterogeneity on hydrophilic and hydrophobic silicas: water and alcohols as probes for H-bonding and dispersion forces, Langmuir 13 (1997) 895–902.

[36] B. Fubini, V. Bolis, A. Cavenago, E. Garrone, P. Ugliengo, Structural and induced heterogeneity at the surface of some SiO2 polymorphs from the enthalpy of adsorption of various molecules, Langmuir 9 (1993) 2712–2720, https://doi.org/10.1021/la00034a034.

[37] S.S. Latthe, R.S.S.S. Sutar, V.S.R.S. Kodag, A.K.V.S. Bhosale, A.M.A.K. Kumar, K.K. A.M. Sadasivuni, R. Xing, S. Liu, Self – cleaning superhydrophobic coatings: potential industrial applications, Prog. Org. Coatings 128 (2019) 52–58.

[38] A.C. Zettlemoyer, H.H.A.C. Hsing, Water on silica and silicate surfaces. III. Hexamethyldisilazane-treated silica surfaces, J. Colloid Interface Sci. 55 (1976) 637–644.

[39] T. Fujimoto, K. Taketoshi, T. Nonaka, Airborne molecular contamination: contamination on substrates and the environment in semiconductors and other industries, in: K.L.M. Rajiv Kohli (Ed.), Dev. Surf. Contam. Clean., William Andrew Publishing., 2008, pp. 197–329.

[40] S. Alexander, J. Eastoe, A.M. Lord, F.A.M. Guittard, A.R. Barron, Branched hydrocarbon low surface energy materials for superhydrophobic nanoparticle derived surfaces, ACS Appl. Mater. Interfaces 8 (2016) 660–666.

[41] G.T. Hermanson, Silane Coupling Agents. Bioconjugate Tech., third ed., Academic Press, Boston, 2013, pp. 535–548.

[42] S.C.C. Wiedemann, P.C.A.S.C. Bruijnincx, B.M.S.C. Weckhuysen, Isostearic acid: a unique fatty acid with great potential, in: Chem. Fuels from Bio-Based Build. Blocks, 2016, pp. 51–78.

[43] M. Armandi, V. Bolis, B. Bonelli, C. Otero Arean, P. Ugliengo, E. Garrone, Silanol-related and unspecific adsorption of molecular ammonia on highly dehydrated silica, J. Phys. Chem. C 115 (2011) 23344–23353.

[44] V. Bolis, C.B. Busco, P. Ugliengo, Thermodynamic study of water adsorption in high-silica zeolites, J. Phys. Chem. B 110 (2006) 14849–14859.

[45] RA.. Horch, N.R.A. Shahid, A.S. Mistry, M.D.A.S. Timmer, A.G.M.D. Mikos, A.R.A. G. Barron, Nanoreinforcement of poly(propylene fumarate)-based networks with surface modified alumoxane nanoparticles for bone tissue engineering, Biomacromolecules 5 (2004) 1900–1998.

[46] S.J. Maguire-Boyle, M.V.S.J. Liga, O.M.V. Li, A.R. Barron, Alumoxane/ferroxane nanoparticles for the removal of viral pathogens: the importance of surface functionality to nanoparticle activity, Nanoscale 4 (2012) 5627–5632.

[47] V.U.V. Bolis, C. Busco, V. Aina, C. Morterra, Surface properties of silica-based biomaterials: Ca species at the surface of amorphous silica as model sites, J. Phys. Chem. C 112 (2008) 16879–16892.

[48] O.P.O. Bera, M. Jovičić, J. Pavličević, B. Pilić, The influence of oxide nanoparticles on the kinetics of free radical methyl methacrylate polymerization in bulk, Polym. Compos. 34 (2013) 1342–1348.

[49] M.S.M.M. Karabela, I.D. Sideridou, Synthesis and study of properties of dental resin composites with different nanosilica particles size, Dent. Mater. 27 (2011) 825–835.

[50] Frankfurt, Technical Bulletin Pigments No. 18, 3rd ed, Degussa AG, 1987.

[51] M. Takeuchi, L. Bertinetti, G. Martra, S. Coluccia, M. Anpo, States of H2O adsorbed on oxides: an investigation by near and mid infrared spectroscopy, Appl. Catal. A Gen. 307 (2006) 13–20.

[52] N.B. Colthup, L.H. Daly, S.E. Wiberley, Introduction to Infrared and Raman Spectroscopy, Third, Academic Press, 1990.

[53] K. Nakamoto, Infrared and Raman Spectra of Inorganic and Coordination Compounds Part B: Applications in Coordination, Organometallic, and Bioinorganic Chemistry, Third, John Wiley & Sons, 2009.

[54] B.L.A.A. Morrow, I.A. Cody, L.S.M. Lee, Infrared studies of reactions on oxide surfaces. 7. Mechanism of the adsorption of water and ammonia on dehydroxylated silica, J. Phys. Chem. 80 (1976) 2761.

[55] P. Ugliengo, V. Saunders, E. Garrone, Silanol as a model for the free hydroxyl of amorphous silica: ab-initio calculations of the interaction with water, J. Phys. Chem. 94 (1990) 2260–2267.

[56] G.B.G.E. Musso, E. Bottinelli, L. Celi, G. Magnacca, G. Berlier, Influence of surface functionalization on the hydrophilic character of mesoporous silica nanoparticles, Phys. Chem. Chem. Phys. 17 (2015) 13882.

[57] L.R.L.F. Scatena, M.G.R.L. Brown, G.R.L.L. Richmond, Water at hydrophobic surfaces: weak hydrogen bonding and strong orientation effects, Science 292 (2001) 908–912.

[58] B.S.B. Fubini, V. Bolis, M. Bailes, F.S. Stone, The reactivity of oxides with water vapor, Solid State Ionics 32–33 (1989) 258–272.

[59] P.N.P. Roach, N.J. Shirtcliffe, M.I. Newton, Progess in superhydrophobic surface development, Soft Matter 4 (2008) 224–240.

[60] Z.S.Z. Wang, W. Yang, F. Sun, P. Zhang, Y. He, X. Wang, D. Luo, W. Ma, G.-C. Sergio, Construction of a superhydrophobic coating using triethoxyvinylsilane-modified silica nanoparticles, Surf. Eng. 35 (2019) 418–425.

[61] X.T.W.T.W.A. Daoud, J.H.J.H. Xin, Synthesis and characterization of hydrophobic silica nanocomposites, Appl. Surf. Sci. 252 (2006) 5368–5371.

[62] Global Safe Handling of Hexamethyldisilazane, (2018) 1–28. https://globalsilicones.org/wp-content/uploads/2020/10/Joint-HMDZ-Safe-Handling-Manual.pdf.